continuous-wave laser, these effects will generally be small compared with those that can be achieved by applying a static electric field.

REFERENCES AND NOTES

1. M. W. Evans, *J. Phys. Chem.* **95**, 2256 (1991).
2. W. S. Warren, S. Mayr, D. Goswami, A. P. West Jr., *Science* **255**, 1683 (1992).
3. R. A. Harris and I. Tinoco Jr., *ibid.* **259**, 835 (1993).
4. M. W. Evans, *Physica. B* **182**, 227 (1992); *ibid.*, p. 237.
5. ———, *Adv. Chem. Phys.* **85** (part 2), 51 (1993).
6. L. D. Barron, *Physica. B* **190**, 307 (1993).
7. A. D. Buckingham and P. J. Stephens, *Annu. Rev. Phys. Chem.* **17**, 399 (1966).
8. W. S. Warren, S. Mayr, D. Goswami, A. P. West Jr., *Science* **259**, 836 (1993).
9. R. A. Harris and I. Tinoco Jr., paper presented at the 5th International Circular Dichroism Conference, Colorado (1993), p. 167.
10. J. P. van der Ziel, P. S. Pershan, L. D. Malmstrom, *Phys. Rev. Lett.* **15**, 190 (1965).
11. The unit vectors **i**, **j**, and **k** in the *x*, *y*, and *z* directions, respectively, are fixed and unaffected by *P* and *T*.
12. A. D. Buckingham, *Adv. Chem. Phys.* **12**, 107 (1967).
13. H. G. Kuhn, *Atomic Spectra* (Longmans, London, 1961), p. 167.
14. A. D. Buckingham, *Proc. Phys. Soc. B* **69**, 344 (1956).

15. L.C.P. is grateful to Trinity College, Cambridge, for the award of a research studentship.

27 December 1993; accepted 8 March 1994

Multiplex Spectroscopy: Determining the Transition Moments and Absolute Concentrations of Molecular Species

Geoffrey J. Germann* and David J. Rakestraw

A procedure is described that uses two spectroscopic techniques, absorption and infrared degenerate four-wave mixing, in tandem (multiplex) to measure the transition dipole moments and absolute concentrations of molecular species in situ. The method is demonstrated by the measurement of the relative transition moments and concentrations of two dissimilar sample gas components, hydrogen chloride and nitrogen dioxide, but is applicable to a wide variety of molecules and, thus, can provide new information for transient molecular species. Further, difficulties in obtaining quantitative information through techniques such as laser-induced fluorescence, coherent anti-Stokes Raman scattering, and degenerate four-wave mixing spectroscopies can be overcome when a multiplex approach is used.

The direct measurement of the absolute concentrations of transient molecular species has long eluded the scientific community. Numerous laser-based diagnostic techniques [laser-induced fluorescence (LIF), coherent anti-Stokes Raman scattering (CARS), multiphoton ionization (MPI), degenerate four-wave mixing (DFWM), and absorption spectroscopy] have been developed to measure the temperatures, velocities, and spatial and temporal profiles of a number of molecular species. None of these techniques can give us information on the absolute number density of molecular species if the line strengths of the probed transitions cannot be determined separately. Absorption spectroscopy is the only technique commonly used to measure molecular transition line strengths, but its usefulness is limited to stable molecular species that can be held at known pressure in a sample cell. Absorption spectroscopy cannot be used to deduce molecular transition line strengths of transient molecular species for which the absolute concentration cannot be determined. Some coherent optical transient methods, such as transient nutation and photon echoes (*1*, *2*), can be used to deduce molecular transition dipole matrix elements, but only if the absolute intensity profile of the probe laser is well known. This inability of the current set of diagnostic probe techniques limits the degree to which chemical systems involving transient species can be understood. Without direct knowledge of the concentrations of transient or free-radical species (which can play pivotal roles in the kinetics and evolution of the chemical system) there is no way to confirm the accuracy of the reaction rates and kinetic models used to describe the chemical system.

The difficulty in measuring either a molecule's transition dipole moment, μ_{21} (or line strength, S_{21}, where $S_{21} \alpha |\mu_{21}|^2$) or absolute number density, N, stems from the fact that spectroscopic probe methods generally require both μ_{21} and N in the equations that describe spectroscopic signal generation. In the case of absorption spectroscopy, the light intensity transmitted through an absorbing medium is given by

$$I_a = I_0 \exp\left(\frac{-\Delta N \ell |\mu_{21}|^2 \omega}{2\Gamma_{21} c \hbar \epsilon_0}\right) \quad (1)$$

at the spectral center of the molecular transition (*3*), where ΔN is the effective molecular number density (that is, the population difference between the quantum states connected in the molecular transition), I_0 is the applied laser intensity, Γ_{21} is the coherence decay rate, ω is the resonant field frequency, ℓ is the sample path length, ϵ_0 is the permittivity of vacuum, c is the speed of light, and $\hbar$ is Planck's constant (h) divided by 2π. Equation 1 involves both S_{21} (or $|\mu_{21}|^2$) and ΔN; consequently, we can never deduce these two quantities by making one measurement. In the case of DFWM spectroscopy (when the applied laser power is low compared to the optical saturation intensity, $I_0 \ll I_{sat}$), the intensity of the signal beam is given by

$$I_s = \left(\frac{2\omega}{\hbar^3 c^2 \epsilon_0^2}\right)^2 (\Delta N \ell_0)^2 \left(\frac{|\mu_{21}|^8}{\Gamma_0^2 \Gamma_{21}^4}\right) I_0^2 I_p \quad (2)$$

at line center (*3*, *4*), where I_p is the intensity of the probe beam, Γ_0 is the quantum-state population decay rate, and ℓ_0 is the path length sampled by the DFWM process. Again, the spectroscopic signal depends on both μ_{21} and ΔN, and so we can never deduce these two quantities independently by making a single measurement.

It is possible to deduce the values of both μ_{21} and ΔN by implementing these two methods of spectroscopy in tandem (multiplex), either simultaneously or sequentially. The method relies on the fact that these two forms of spectroscopy involve the same quantities but have different functional dependences on the two variables of interest, μ_{21} and ΔN. In this case, Eqs. 1 and 2 can be treated as simultaneous equations and solved to determine both μ_{21} and ΔN separately. In the present work we measure the molecular transition dipole moment and absolute concentration of HCl by the simultaneous recording of infrared (IR) DFWM and absorption spectra. We include NO_2 in the gas sample mixture with HCl to serve as an in situ calibrant. We record the IR DFWM and absorption spectra of the HCl-NO_2 combined gas mixture and deduce the μ_{21} and ΔN values of HCl relative to those of NO_2. This method simplifies the experimental procedure, and Eqs. 1 and 2 give

$$|\mu_{21}|_{HCl} = \sqrt[4]{\frac{R_{DFWM}}{R_{abs}^2}} \frac{\Gamma_0^{HCl}}{\Gamma_0^{NO_2}} |\mu_{21}|_{NO_2} \quad (3)$$

and

$$\Delta N_{HCl} = \sqrt{\frac{R_{abs}^4}{R_{DFWM}}} \frac{\Gamma_0^{NO_2}}{\Gamma_0^{HCl}} \Delta N_{NO_2} \quad (4)$$

Sandia National Laboratories, Combustion Research Facility, Livermore, CA 94550, USA.

*To whom correspondence should be addressed.

where

$$R_{abs} = \frac{\ln(I_a^{HCl}) - \ln(I_0^{HCl})}{\ln(I_a^{NO_2}) - \ln(I_0^{NO_2})} \quad (5)$$

and

$$R_{DFWM} = \frac{I_s^{HCl}}{I_s^{NO_2}} \quad (6)$$

A schematic of the experimental apparatus is shown in Fig. 1 (5, 6). An injection-seeded Nd:YAG laser is used to pump an optical parametric oscillator-amplifier (OPO-OPA). The OPO-OPA provides 1 to 3 mJ of IR light tunable from 2900 to 3000 cm^{-1}. A pulsed wavemeter is used to measure the IR wavelength as the frequency is scanned. The IR beam is split into two beams of roughly equal intensity that are directed into and crossed within a sample cell, at an angle of ~4°. Sample gases of HCl and NO_2 as well as N_2 buffer gas are introduced into the sample cell, in the ratio of ~1:3:2000, to a total pressure of 200 torr. One of the IR input beams, the forward pump beam, ω_f, is retroreflected to provide ω_b, the backward pump beam in the DFWM process. The other IR beam, ω_p, the probe beam, is allowed to continue out of the sample cell and is directed into an IR detector and recorded as a function of wavelength. This value provides the absorption spectrum in the experiment (7). The phase conjugate DFWM signal beam, ω_s, is generated counter-propagating to ω_p. The signal beam is split from ω_p by an IR beam splitter and directed into an InSb detector. The intensity of ω_s is recorded as a function of wavelength simultaneously with the absorption measurement. The DFWM spectrum is obtained by division of the measured DFWM signal-beam intensity by the third power of the transmitted beam intensity (the absorption measurement) (6). This function corrects for any decrease in the DFWM signal resulting from absorption of the pump, probe, and signal beams by the gas sample. The intensity of the beams is kept low to avoid optical saturation and provide that Eq. 2 accurately describes the DFWM signal intensity.

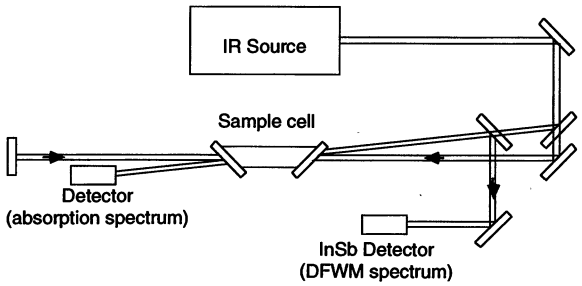

Fig. 1. An experimental schematic of the apparatus used to record IR DFWM and absorption spectra simultaneously.

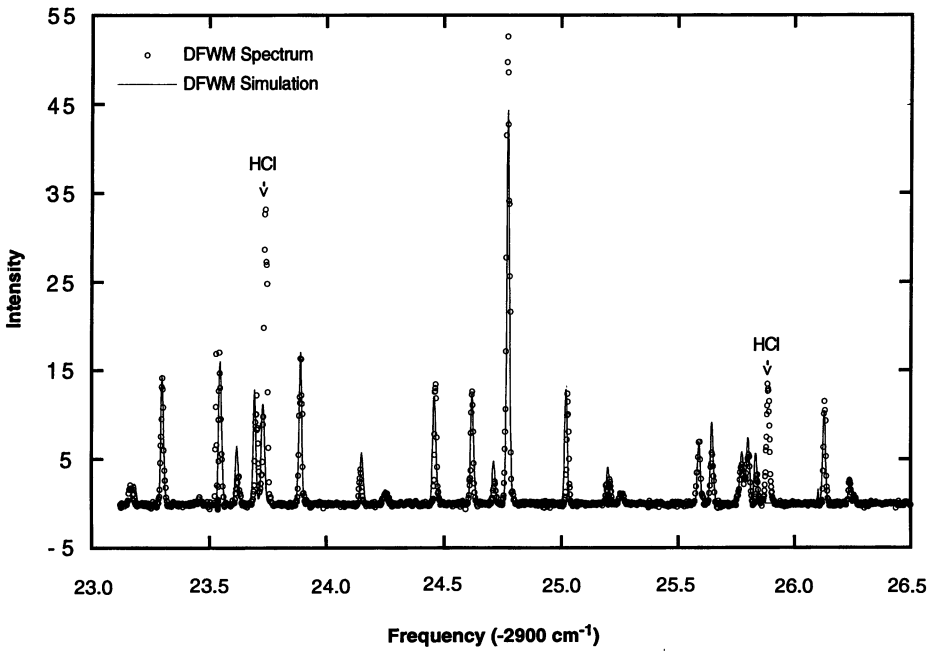

Fig. 2. A partial R-branch rovibrational DFWM spectrum of the (101)-(000) band of NO_2 recorded with low laser intensities (given in relative units). The solid line represents the spectrum calculated with a theoretical model that corresponds with Eq. 2 for $I_0 \ll I_{sat}$. Features that do not appear in the calculated spectrum are due to HCl.

Figure 2 shows a partial rovibrational R-branch spectrum for the (101)-(000) band of NO_2. We note that to model the DFWM spectrum of NO_2 accurately, the population and coherence decay rates, Γ_0 and Γ_{21} in Eq. 2, must be known. For N_2 buffer-gas pressures near 200 torr, Γ_0 and Γ_{21} are dominated by collision processes and are given by the N_2 pressure-broadening coefficient, b_p, for NO_2 (8). The solid line represents the best fit to the data from a stationary absorber model (9, 10), which corresponds with Eq. 2 for $I_0 \ll I_{sat}$. Features not shown in the calculated spectrum are due to HCl in the sample cell. The data are modeled quite well in the figure, and so we infer that Eq. 2 accurately describes the spectroscopic behavior of NO_2 in this experiment.

In Fig. 3, we show a section of the NO_2 R-branch DFWM spectrum together with the simultaneously obtained absorption spectrum. The spectra include the R(1) rovibrational transition of HCl. The solid lines show successive attempts to fit the HCl R(1) feature with different combinations of the μ_{21} and ΔN values. Each contour in the figure represents a 10% increment to the value of μ_{21}. Here again, Γ_0 and Γ_{21} for HCl are dominated by N_2 collision processes [b_p = 0.089 ± 0.001 cm^{-1}/atm (11)]. It is important to note that each of the simulated DFWM spectra in Fig. 3 is consistent with the same absorption spectrum, shown in the figure. The differences in the DFWM and absorption spectra result from the different functional dependences of Eqs. 1 and 2 on μ_{21} and ΔN. A value of μ_{21} = 0.079 ± 0.008 D for HCl R(1) is required to fit both the absorption and DFWM measurements simultaneously [a value consistent with that given by Eq. 3, where μ_{21} = 0.0485 ± 0.0005 D for NO_2 (12)]. Changing μ_{21} by 10% alters the simulated spectrum markedly and results in a clear discrepancy between the measured and simulated DFWM signal intensities. This value of μ_{21}, 0.079 ± 0.008 D for HCl, agrees well with the results of other measurements; a value for μ_{21}^{HCl} of 0.0729 D was obtained by more traditional methods (13). The value of ΔN for HCl R(1) obtained from the spectral fit in Fig. 3 (and equivalently calculated with Eq. 4) represents the absolute number density of HCl molecules in the $J = 1, v = 0$ quantum state relative to that of NO_2 in the quantum states observed in the spectrum. The accuracy of this value is confirmed by the absorption spectrum, which is an absolute measurement. We cannot provide a separate confirmation of this value because the amount of static HCl in the sample cell decreased measurably during data collection, presumably the result of reaction with

the cell walls. We are currently using flowing gases to improve the stability of the sample gas ratio.

In Fig. 4, we again show the section of the NO_2 R-branch DFWM spectrum (presented in Fig. 3) together with the simultaneously obtained absorption spectrum. In this case, the solid lines show successive attempts to fit the HCl R(1) feature in the absorption spectrum with different combinations of μ_{21} and ΔN. Each of the simulated absorption spectra is consistent with the same DFWM spectrum, shown in the figure. Just as in Fig. 3, each successive simulation of the absorption spectrum represents a one SD, 10%, change in μ_{21}. This change demonstrates that the limiting source of spectral uncertainty is attributable to the absorption measurement because Eq. 1 has a much weaker functional dependence on μ_{21} and ΔN than does Eq. 2. Although only ~5% uncertainty in the experimental measurements is attributable to spectral noise, the N_2 b_p of NO_2 is only determined to within ±5%. For these reasons, a 10% overall uncertainty in the measurements is given.

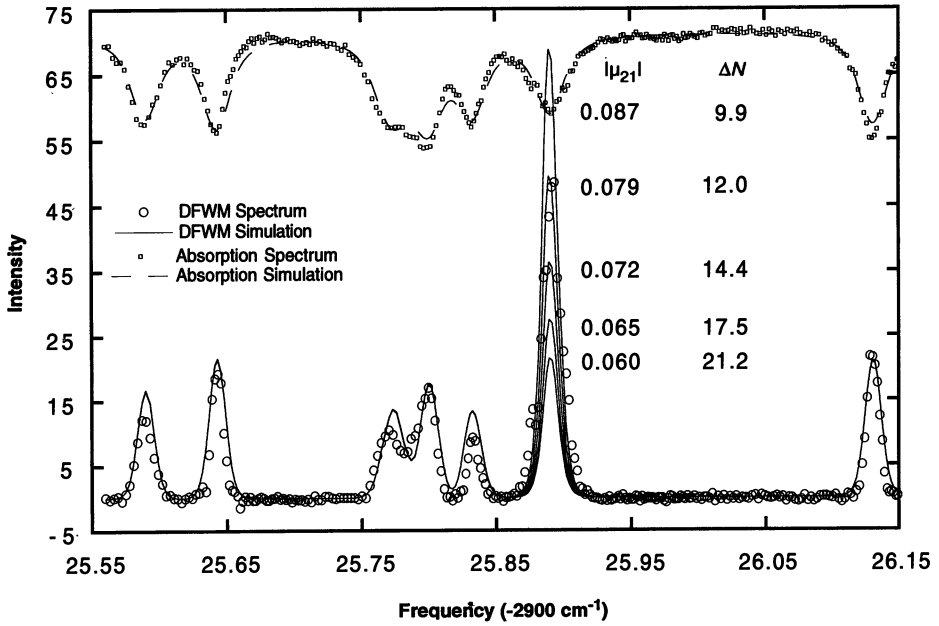

Fig. 3. The NO_2 (101)-(000) R-branch DFWM and absorption spectra. The spectra were recorded simultaneously and include the R(1) rovibrational transition of HCl. The solid lines show successive attempts to fit the HCl R(1) feature in the DFWM spectrum with a stationary absorber model that corresponds with Eq. 2 at low laser intensity, $I_0 \ll I_{sat}$. Each contour is consistent with the absorption spectrum shown in the figure and represents a 10% increment to the value of μ_{21}.

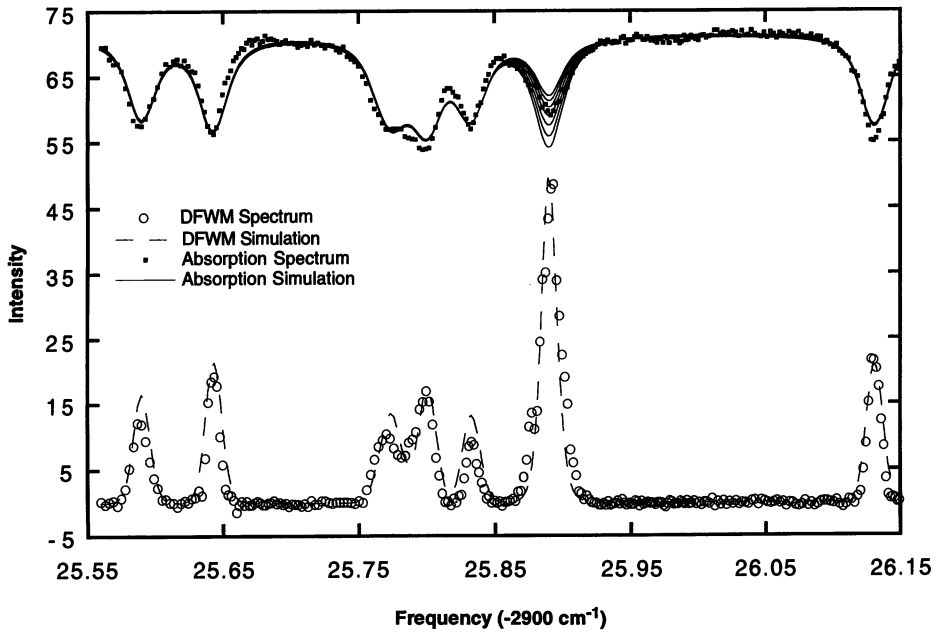

Fig. 4. The NO_2 (101)-(000) R-branch DFWM and absorption spectra. The spectra were recorded simultaneously and include the R(1) rovibrational transition of HCl. The solid lines show successive attempts to fit the HCl R(1) feature in the absorption spectrum with a stationary absorber model that corresponds with Eq. 2 at low laser intensity, $I_0 \ll I_{sat}$. Each contour is consistent with the DFWM spectrum shown in the figure and represents a 10% increment to the value of μ_{21}.

This multiplex investigation using DFWM and absorption spectroscopy in tandem can accurately measure the molecular transition dipole moments and, thus, the absolute concentrations of molecules detectable by these two forms of spectroscopy. This same procedure can be expected to measure μ_{21} and ΔN accurately for transient molecular species, about which we have limited knowledge. We are now pursuing an experiment to measure the transition dipole moments and absolute concentrations of hydrocarbon species (CH_3, CH_2, and CH) present in chemical vapor deposition processes and low-pressure flames. Such measurements have to date been impossible for any one form of spectroscopy independently and can vastly improve our knowledge of chemical processes involving transient or free-radical species.

It is important to point out that this process is not unique to DFWM and absorption spectroscopy. In Fig. 5 we show schematics for other multiplex experiments that could solve fundamental problems of interpretation suffered by each one of the spectroscopies

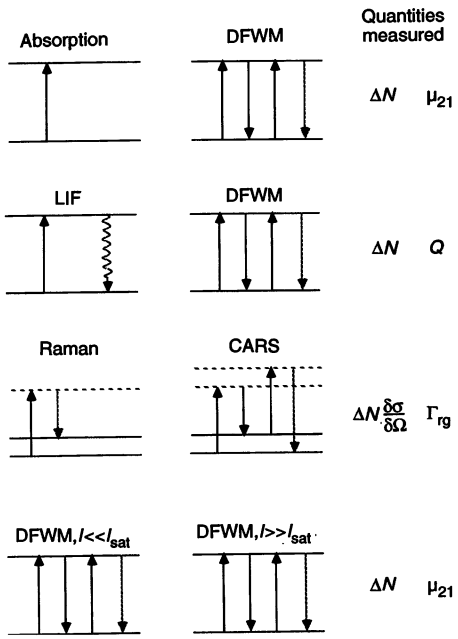

Fig. 5. Schematics for multiplex spectroscopy experiments.

involved. The first diagram shows the processes used in the present work. The second diagram shows schematics for the DFWM and LIF processes. These two techniques involve the same molecular transition (and thus the same molecular quantum-state population density), but each of these processes has a different functional dependence on the molecular quantum-state quenching rate, Q (*14*). This difference can be exploited to solve for Q, and by so doing, the need to measure Q separately and for each molecular collision partner can be avoided. This multiplex experiment would enable LIF, a very sensitive spectroscopic technique, to determine absolute concentrations of molecular species. The third diagram shows schematics for Raman and CARS spectroscopies. Raman and CARS involve the same two-photon molecular transition, but each of these processes has a different functional dependence on the molecular transition linewidth, Γ_{rg} (*15, 16*). The two formulas that describe Raman and CARS spectroscopic signal generation can be used as simultaneous equations to determine Γ_{rg}, even if the linewidth of the probe laser greatly exceeds the linewidth of the spectroscopic transition. As a final example, we show two diagrams for DFWM spectroscopy. This technique can be implemented as a diagnostic probe in either the high or low optical power limits (*3, 4*). The fact that the DFWM signal generated in each of these power limits has a different functional dependence on μ_{21} indicates that DFWM can be used to find μ_{21} and ΔN, if this aspect of the technique is exploited. Clearly, numerous unexplored opportunities exist to exploit current spectroscopies in new ways to make hitherto unattainable measurements.

REFERENCES AND NOTES

1. H. Walther, *Laser Spectroscopy of Atoms and Molecules*, H. Walther, Ed. (Springer-Verlag, Heidelberg, 1976).
2. W. Demtröder, *Laser Spectroscopy Basic Concepts and Instrumentation* (Springer-Verlag, Heidelberg, 2nd printing, 1982).
3. P. H. Vaccaro, *Adv. Phys. Chem.*, in press.
4. R. L. Farrow and D. J. Rakestraw, *J. Opt. Soc. Am. B* **9**, 1770 (1992).
5. G. J. Germann, A. McIlroy, T. Dreier, R. L. Farrow, D. J. Rakestraw, *Ber. Bunsenges. Phys. Chem.* **97**, 1630 (1993).
6. G. J. Germann and D. J. Rakestraw, unpublished results.
7. The absorption spectrum is taken as the ratio of the transmitted laser power to the input laser power to correct for shot-to-shot laser-power fluctuations.
8. The b_p value of 0.074 ± 0.004 cm^{-1}/atm was used for the (101)-(000) vibrational band of NO_2. This value was obtained from the average of the b_p values for the (010)-(000) and (001)-(000) vibrational bands of NO_2, 0.071 ± 0.004 [R. D. May and C. R. Webster, *Geophys. Res. Lett.* **17**, 2157 (1990)] and 0.077 ± 0.006 cm^{-1}/atm [V. M. Devi *et al.*, *J. Mol. Spectros.* **84**, 234 (1980)], respectively.
9. R. L. Abrams, J. F. Lam, R. C. Lind, D. G. Steel, P. F. Liao, in *Optical Phase Conjugation*, R. A. Fisher, Ed. (Academic Press, New York, 1983), p. 211.
10. R. L. Abrams and R. C. Lind, *Opt. Lett.* **2**, 94 (1978).
11. A. S. Pine and J. P. Looney, *J. Mol. Spectros.* **122**, 41 (1987).
12. R. A. Toth and R. H. Hunt, *ibid.* **79**, 182 (1980).
13. A. S. Pine, A. Fried, J. W. Elkins, *ibid.* **109**, 30 (1985).
14. P. M. Danehy, E. J. Friedman-Hill, R. P. Lucht, R. L. Farrow, *Appl. Phys. B* **57**, 243 (1993).
15. S. A. J. Druet and J.-P. E. Taran, *Prog. Quantum Electron.* **7**, 1 (1981).
16. A. C. Eckbreth, *Laser Diagnostics for Combustion Temperature and Species*, A. K. Gupta and D. G. Lilley, Eds. (Abacus Press, Cambridge, MA, 1988).

17. We thank R. L. Farrow for developing the spectral simulation software used to analyze the experimental data, G. A. Hux for technical support, and R. L. Farrow and P. H. Paul for useful discussions. Supported by the U.S. Department of Energy, Office of Basic Energy Sciences, Division of Chemical Sciences.

8 February 1994; accepted 9 May 1994

Higher Order Self-Assembly of Vesicles by Site-Specific Binding

Shivkumar Chiruvolu, Scott Walker, Jacob Israelachvili, Franz-Josef Schmitt, Deborah Leckband, Joseph A. Zasadzinski*

The association of lipid molecules into spherical vesicles in solution as a result of nonspecific intermolecular forces constitutes a primary self-assembly process. Such vesicles can undergo a secondary self-assembly into higher order structures in a controlled and reversible manner by means of site-specific ligand-receptor (biotin-streptavidin) coupling. Cryoelectron microscopy shows these structures to be composed of tethered, rather than adhering, vesicles in their original, unstressed state. In contrast, vesicles aggregated by nonspecific, such as van der Waals, forces are deformed and stressed, producing unstable structures. Vesicle association by site-specific binding provides a practical mechanism for the production of stable, yet controllable, microstructured biomaterials.

Much of the recent interest in self-assembling structures, in which surfactant or polymeric molecules in solution spontaneously assemble into large, thermodynamically stable structures with well-defined geometries, springs from the close association of this process with living systems (*1–4*). The simplest and most studied of these biomimetic structures are unilamellar vesicles, which are single, spheroidal bilayer shells encapsulating an aqueous interior (*2–4*). Proteins and other biologically active molecules can be incorporated into the vesicle bilayer or interior, thereby serving as models of biological cells (*2–4*). Vesicles are also currently being developed for drug delivery applications (*3*). However, the analogy to living systems is, as yet, incomplete. There are invariably several levels of self-assembly in even the simplest cell or tissue. The next, or secondary, level of self-assembly is achieved through the specific, but reversible, association of vesicles into stable multivesicle aggregates by means of ligand-receptor coupling. Such structures should serve as idealized models for biological tissues, and their spontaneous formation in the laboratory could lead to new methods for processing artificial tissues and "soft" composite materials.

The self-assembly of molecules and small aggregates in solution into larger structures is brought about by a number of attractive forces: van der Waals, ion-binding, hydrophobic, polymer bridging, and depletion forces, as well as lock-and-key type interactions (*5*). Apart from the last, all of these forces may be considered nonspecific because they act indiscriminately between all parts of the particles. The resulting adhesion is usually described in terms of the adhesion energy, W, which is the reversible work done on bringing two surfaces of unit area into adhesive contact. By definition, $W = 2\gamma$, where γ is the surface or interfacial energy per unit area (*5*).

When two soft colloidal particles or vesicles aggregate as a result of nonspecific forces, they deform elastically to increase their mutual area of contact as much as possible (similar to the mutual flattening of two adhering soap bubbles). Such vesicle deformations can be imaged by electron microscopy. For example, phosphatidylcholine (PC) vesicles can be induced to aggregate by stressing them osmotically (Fig. 1), which suppresses the repulsive undulation force and enhances the attractive hydrophobic force between them (*6, 7*). Similar deformed structures are produced by other types of nonspecific surface forces, for example, when negatively charged vesicles are aggregated by addition of calcium ions to the solution (*8, 9*). These deformations cause large elastic strains and stresses on bilayers and membranes, which result in

Department of Chemical Engineering, University of California, Santa Barbara, CA 93106, USA.

*To whom correspondence should be addressed.